Natural ageing clustering under different quenching conditions in an Al-Mg-Si alloy

Zi Yang[1,*], Xiaohe Jiang[1], Xingpu Zhang[1], Meng Liu[1], Zeqin Liang[2], David Leyvraz[2], John Banhart[1]

[1]Helmholtz-Centre Berlin for Materials and Energy, Hahn-Meitner-Platz 1, 14109 Berlin, Germany

[2]Novelis R&T Centre Sierre, Route des Laminoirs 15, 3960 Sierre, Switzerland

[*] Corresponding: zi.yang@helmholtz-berlin.de

Abstract

During quenching of aluminium alloys from the solutionising temperature vacancies are partially conserved as excess vacancies, partially lost to vacancy sinks, the exact fractions depending on the cooling rate. Positron lifetime measurements in samples from interrupted quenching experiments reveal that vacancies are lost during cooling down to 200 °C, after which solute atoms start to form clusters down to 20 °C. Slow cooling leads to 1 to 2 orders of magnitude lower excess vacancies than fast cooling. Since quenched-in vacancies are crucial for natural ageing (NA) in Al-Mg-Si alloys it is surprising to find just small differences between the NA hardening kinetics after different quenches. Specifically, hardening rates differ only in the initial stage (<100 min), after which they are almost identical for NA up to ~1 year. This suggests that interactions between vacancies and early-stage solute clusters help equalising the free vacancy fractions in differently quenched samples.

Keywords: Al-Mg-Si alloy; solute clustering; quench rate; natural ageing

Precipitation hardening is the most important technique to increase the strength of Al-Mg-Si alloys (6000 series). In practice, strength enhancement is mainly achieved during artificial ageing (AA), which typically takes place at temperatures around 180 °C. The importance of natural ageing (NA) at 'room temperature' lies in the fact that its presence markedly modifies the subsequent AA kinetics 'positively' [1, 2] or 'negatively' [2, 3], depending on the alloy composition and temperature of AA. Although the exact mechanisms are still debated, it is generally accepted that the effect is related to the clusters formed during NA. Thus, investigating the clustering process and the properties of the clusters in Al-Mg-Si alloys is of great practical relevance.

Diffusion of solutes at 'room temperature' under equilibrium conditions is too slow to cause the observed rapid NA clustering [4] and non-equilibrium excess vacancies quenched-in from the solutionising temperature play a crucial role as the diffusion rate scales with the vacancy site fraction [5-7]. Previous studies have shown that clustering can be retarded by adding vacancy-binding elements, e.g. Sn or In [8-10], or applying modified quenching procedures to enable the excess vacancies to move to sinks at high temperature where their mobility is high [11]. However, how clustering kinetics is exactly related to the excess vacancy site fraction remains unclear.

In this study, positron annihilation lifetime spectroscopy (PALS) was applied to probe vacancies, as positrons show markedly higher lifetimes where the electron density is lower, e.g. at open volume defects such as vacancies. Different starting vacancy site fractions were created by varying the quenching conditions. The subsequent clustering phenomena during NA were characterised by measuring hardness and positron lifetime. This work intends to clarify how the vacancy site fraction changes during quenching and how the vacancy fraction after quenching affects NA clustering kinetics.

The investigated alloy AA6014 was provided by Novelis Switzerland and contains 0.65% Mg, 0.60% Si, 0.18% Fe, 0.08% Mn, 0.12% Cu, all in wt.%, as measured by optical emission spectroscopy. Samples were sliced into pieces of ~10×10×1 mm^3 size and solutionised at 540 °C for 1 h in an air circulation furnace before being subjected to quenching procedures of two different types: In the first (Q1), samples were quenched in one step either in ice-water (IWQ), by the air flow of a ventilator (VC, see supplementary Fig. S1) or in resting air (AC), the latter two at ~20 °C. In the second (Q2), the processes of VC or AC were not completed but interrupted at a given target temperature by applying a subsequent fast quench in ice-water. The samples treated in this way are labelled 'VC_*x*' or 'AC_*x*', where *x* stands for a target temperature ranging from 100 °C to 400 °C and controlled within ±15 °C for VC and ±5 °C for AC. The temperature evolution during cooling was determined by a thermocouple inserted into a hole drilled into the side of a dummy sample and was assumed to be the same for all other samples. Typical cooling curves are given in Fig. 1. Average cooling rates from 533 °C to 250 °C were >980 Ks^{-1} for IWQ, ~27 Ks^{-1} for VC, and ~5 Ks^{-1} for AC, respectively. Natural ageing was performed in a Peltier-cooled incubator at 20 ± 0.1 °C for hardness samples, or in an air-conditioned room at 20 ± 2 °C for in-situ PALS measurements.

Brinell hardness was measured on a Qness 60M tester using a load of 10 kg and a tungsten carbide indenter of 1 mm diameter. Eight indentations were performed on each sample and averaged. The corresponding standard deviation was <1 HBW for >98% of the measurements. PALS measurements were performed using a fast-fast coincidence system [12]. Positrons were produced by a ^{22}Na source enveloped in Kapton foil, which was sandwiched by two identically processed alloy samples during measurement. The spectrometer had a resolution (FWHM) of ~200 ps, and a

count rate ~600 s^{-1}. Software LT9 was used to fit the lifetime spectra and determine one-component lifetimes.

Hardnesses of the alloy after various Q1-type quenches and during NA are presented in Fig. 2. Similar hardnesses in the as-quenched states are found. During ageing, pronounced hardening is observed for all quenching conditions, with a lower hardening response seen for samples subjected to slower quenching. The hardening rates throughout NA are evaluated by fitting the data with the Starink-Zahra equation [13] and taking derivatives. The fits yield an R^2>0.998 for all three curves, better than JMAK-type equations often used for representing precipitation kinetics. For all quenching conditions, hardening rates are high in the initial period of NA and then decrease markedly. Differences in hardening rates are found only in the initial stage (<100 min), where the absolute hardening effect is still small compared to the total hardness increase during extended NA. In other words, the stage of most pronounced hardening (> 100 min) is actually independent of quenching.

PALS provides more insights into the microstructure evolution. Fig. 3 presents one-component positron lifetimes (τ_{1C}) in the samples after various quenches (Q1) and during NA. Such signals, in line with previous results by Strobel et al. [14], represent a weighted average of positron lifetimes in various microstructural features which, in the current systems and for the ageing processes applied, are mono-vacancies (typical lifetime ~245 ps), solute clusters (210 – 220 ps), and bulk Al (≤160 ps) [15]. The course of lifetime evolution during NA features various stages, which have been interpreted as vacancy loss and formation of Si-rich clusters (Stage II), Mg enrichment in clusters (Stage III), and cluster coalescence or internal ordering (Stage IV) [15, 16]. Lifetime increase in stage I is still not fully understood but is supposed to be linked to clustering because such increase is not observed in non-clustering binary Al-Mg alloys (supplementary

Fig. S2). After NA for ~100 min, the similar positron lifetimes in all three samples suggest saturated trapping of positrons in solute clusters.

The different initial lifetimes during NA denote very distinct quenched states. After direct quenching in ice-water, a positron lifetime of 232 ps is obtained in agreement with previous observations [16-19]. Such high τ_{1C} points at a dominant contribution of a vacancy-related component. For the two slower-quenched states, positron lifetime is much lower (~217 ps). Since both vacancy loss and cluster formation are able to drive lifetime to such a value, it is hard to extract the information associated to initial vacancy site fraction in these states. Therefore, more details about the process of slow quenching are required, which is why Q2-type quenches were applied. After the interruption of slow quenching by fast quenching in ice-water, it is assumed the microstructure at the interruption temperature is largely preserved. By collecting the initial positron lifetimes during NA (supplementary Fig. S3), the positron lifetime evolutions during VC and AC are obtained indirectly (Fig. 4). Due to a fast lifetime development in the initial minutes of NA, positron lifetime is extrapolated to zero NA time to approximate the state directly after quenching. For both quenching routes, τ_{1C} first decreases and then increases, with a transition between the stages at 200 °C regardless whether values extrapolated to zero NA time or values after a few minutes of NA are considered (broken and full lines, respectively).

The drop of τ_{1C} during slower cooling down to 200 °C (Fig. 4) is a clear evidence of vacancy site fraction reduction due to annihilation at sinks. The observed precipitate formation on dispersoids during slow quenching (supplementary Fig. S4) contributes little to the change of positron lifetime, because the number density of precipitates, even if growing on every dispersoid (~10^{18} m^{-3} [20, 21] = site fraction 1.6×10^{-11}), is too low to trap enough positrons. A lower positron lifetime for AC_200 than VC_200 indicates higher vacancy losses during slower quenching. During VC and

AC, most excess vacancies have annihilated when reaching 200 °C, so that positrons annihilate mostly in the bulk, yielding lifetimes very close to 160 ps. This is very different from what is observed during NA, see Fig. 3, where the positron lifetime is always much higher than 160 ps due to the presence of a dense population of clusters that trap most positrons. A rough estimation (see supplementary Sec. SE) suggests that the vacancy site fraction drops to 1/33 or 1/66 of its original value after solutionising during VC or AC to 200 °C, respectively. These vacancy site fractions are maximum values since any cluster formed during quenching already above 200 °C would also help to keep the measured positron lifetime above 160 ps.

Further cooling to below 200 °C increases τ_{1C}, indicating the formation of clusters or nuclei of precipitates since the vacancy site fraction cannot re-increase. This argument is supported by the final lifetime (~217 ps) that falls into the typical positron lifetime range (210 to 220 ps) for annihilation in clusters. However, these clusters barely harden the alloy (supplementary Fig. S4d).

As a first result, we have therefore shown from the perspective of positron lifetimes that the slow quenching process is divided into a vacancy-loss dominated regime and a clustering regime (with possibly some overlap).

Next, it has to be explained how such large initial differences in vacancy site fraction after different quenched (at least 1–2 orders of magnitude apart) result in just a small hardening difference during NA. The clusters formed during quenching have little impact on NA clustering since the samples with hardly any clusters (AC_200) show similar hardening as samples with clusters (AC, see Fig. 2). The influence of solute supersaturation reduction associated precipitation during quenching ([22-24], and supplementary Fig. S4) on NA clustering kinetics is disregarded here based on two considerations: 1) NA clustering is more governed by vacancies; 2) a lower solute

supersaturation after AC (or VC) than after IWQ would further delay NA hardening, thus increasing the expected difference instead of decreasing it.

If the difference in quenched-in vacancy site fractions remained during NA, it would result in a proportional delay of clustering kinetics such as observed in Al-Zn alloys [25]. Clearly, this is not the case here as the hardening rates differ only in the beginning but later are equalised, suggesting that the vacancy site fraction difference is eliminated. Thus, interactions between vacancies and other microstructural features must play an important role in such equalisation. Here, we analyse three types of interactions, namely between vacancy and vacancy sinks (vacancy annihilation), between vacancy and vacancy (vacancy clustering), and between vacancy and solute clusters (vacancy trapping).

Vacancy annihilation down to the equilibrium value at 20 °C would eliminate any difference but cannot be the case here because, 1) hardening in the early stage is limited and non-equilibrium vacancies are still required to explain the following strong hardening; 2) vacancy annihilation simulations show that the time to equilibrium is 3 orders of magnitude longer than 100 min [26, 27]. Therefore, there must be other mechanisms that remove vacancies faster from a high-vacancy than from a low-vacancy configuration.

Vacancy clusters or their condensed structure, dislocation loops, were reported in quenched alloys [28-30] and after NA [31, 32]. A higher excess vacancy site fraction due to higher solutionising temperatures or higher quench rates would increase the number density and the total number of vacancies in dislocation loops [29, 33-35]. Theoretically, this mechanism could provide an efficient way to eliminate vacancies faster in the faster-quenched samples. However, recent investigations suggest that alloys with >0.1% Mg promotes the preservation of mono-vacancies instead of their clustered state in the alloy [36]. Thus, vacancy cluster formation is not regarded as

the dominant, if it is one, mechanism to equalise the vacancy site fractions in fast- and slow-quenched samples.

Interactions between vacancy and solute atoms play an important role in solute clustering. Zurob et al. proposed that the kinetics of clustering is limited by the probability of a vacancy escaping from a solute cluster, which can be represented as $p \propto \exp\left(-\frac{\alpha n E_b}{kT}\right)$, with n the number of solute atoms in the cluster, E_b the binding energy of a single solute and a vacancy, and α a constant [37]. The escape of a vacancy from a cluster in their model is simplified as a number of consecutive jumps and each jump follows the dissociation of the solute-vacancy pair. Therefore, the binding energy of vacancy and cluster is proportional to sum of all solute-vacancy pair binding energies. Zurob's model suggests that as the clusters grow, vacancies are harder to de-trap from the clusters and further assist the diffusion of other solutes. This explains the low clustering rate in the late stage of NA but not the vacancy equalisation in the early stage. In their model, however, one solute type is considered while clusters in 6xxx alloys normally consist of both Si and Mg atoms, and Si-vacancy binding is widely argued to be stronger than Mg-vacancy [38-41]. Therefore, clusters of different chemistry are supposed to possess different interactions with vacancies, with higher binding energies for Si-richer clusters. This proposition has recently been underlined by Peng et al. [41], who calculated the binding energy between a vacancy and different solute dimers, smallest solute clusters formed at very initial NA [42]. It is shown that Si-Si clusters indeed have a much higher binding energy (0.14 eV) with a vacancy than Mg-Si (0.09 eV) and Mg-Mg (0.05 eV) clusters and individual Mg or Si atoms (0.01 and 0.06 eV, resp.) [41]. Moreover, it is argued that an unstable Si-Si configuration can be stabilised by involving one vacancy [41], suggesting that more vacancies can prompt the formation of more such configurations. Owing to a faster diffusion of Si than Mg, clusters during NA are claimed to be initially Si-richer and later enrich in Mg [16,

43]. Therefore, with the consideration of cluster chemistry evolution in Zurob's model, we can interpret the vacancy equalisation qualitatively by a faster and stronger clustering of Si-rich clusters under higher vacancy site fraction after faster quenching, which in turn traps vacancies strongly and slows down clustering until it is the same as in slower-quenched samples. This also explains the constant hardening offset in Fig. 2.

In summary, we have investigated quenching processes at three different rates (IWQ>VC>AC) and the NA clustering kinetics after. We find:

- During VC and AC quenches, positron lifetimes first decrease and then increase. The former is attributed to vacancy annihilation, while the latter is associated with solute clustering. Thus, the microscopic phenomena during quenching take place in two stages with a transition temperature at 200 °C.
- Vacancy site fractions after VC and AC quenches are estimated at least 1 to 2 orders of magnitude lower than after IWQ. This gives rise to different hardening responses only in the early stage NA (<100 min), after which the hardening rate is independent of the quenching condition.
- The rapid equalisation of vacancy site fractions after various quenching conditions is mainly correlated with the interaction between vacancies and solute clusters. More Si-rich clusters are formed in the early stage of NA after faster quenching, which in turn trap vacancies more efficiently, thus substantially reducing the mobile vacancy site fraction.

Ackowledgements

The authors would like to thank Christiane Förster for preparing the TEM samples and Claudia Leistner for her help in the construction of the ventilator cooling device.

References

[1] C.S.T. Chang, I. Wieler, N. Wanderka, J. Banhart, Ultramicroscopy 109(5) (2009) 585-592.
[2] S. Pogatscher, H. Antrekowitsch, H. Leitner, T. Ebner, P.J. Uggowitzer, Acta Materialia 59(9) (2011) 3352-3363.
[3] J. Banhart, C.S.T. Chang, Z.Q. Liang, N. Wanderka, M.D.H. Lay, A.J. Hill, Advanced Engineering Materials 12(7) (2010) 559-571.
[4] H.K. Hardy, Journal of the Institute of Metals 79(11) (1951) 321-369.
[5] T. Federighi, Acta Metallurgica 6 (1958) 379-381.
[6] A. Kelly, R.B. Nicholson, Progress in Materials Science 10 (1963) 149-391.
[7] P. Dumitraschkewitz, P.J. Uggowitzer, S.S.A. Gerstl, J.F. Löffler, S. Pogatscher, Nature Communications 10 (2019) 4746.
[8] S. Pogatscher, H. Antrekowitsch, M. Werinos, F. Moszner, S.S.A. Gerstl, M.F. Francis, W.A. Curtin, J.F. Löffler, P.G. Uggowitzer, Physical Review Letters 112 (2014) 225701.
[9] M. Liu, X. Zhang, B. Körner, M. Elsayed, Z. Liang, D. Leyvraz, J. Banhart, Materialia 6 (2019) 100261.
[10] M. Werinos, H. Antrekowitsch, T. Ebner, R. Prillhofer, W.A. Curtin, P.J. Uggowitzer, S. Pogatscher, Acta Materialia 118 (2016) 296-305.
[11] S. Pogatscher, E. Kozeschnik, H. Antrekowitsch, M. Werinos, S.S.A. Gerstl, J.F. Loffler, P.J. Uggowitzer, Scripta Materialia 89 (2014) 53-56.
[12] M. Liu, Clustering kinetics in Al-Mg-Si alloys investigated by positron annihilation techniques, PhD thesis, Technische Universität Berlin, Berlin, 2014.
[13] M.J. Starink, A.M. Zahra, Thermochimica Acta 292(1-2) (1997) 159-168.
[14] K. Strobel, M.A. Easton, M.D.H. Lay, P.A. Rometsch, S. Zhu, L. Sweet, N.C. Parson, A.J. Hill, Metallurgical and Materials Transaction A 50A (2019) 1957-1969.
[15] M. Liu, J. Cizek, C.S.T. Chang, J. Banhart, Acta Materialia 91 (2015) 355–364.
[16] J. Banhart, M.D.H. Lay, C.S.T. Chang, A.J. Hill, Physical Review B 83(1) (2011) 014101.
[17] J. Buha, P.R. Munroe, R.N. Lumley, A.G. Crosky, A.J. Hill, Positron studies of precipitation in 6061 aluminium alloys, in: B.C. Muddle, A.J. Morton, J.-F. Nie (Eds.) International Conference on Aluminium Alloys (ICAA-9), Institute of Materials Engineering Australia, Brisbane, Australia, 2004, pp. 1028-1033.
[18] M.D.H. Lay, H.S. Zurob, C.R. Hutchinson, T.J. Bastow, A.J. Hill, Metallurgical and Materials Transactions A 43A(12) (2012) 4507-4513.
[19] M. Madanat, M. Liu, J. Banhart, Acta Materialia 159 (2018) 163-172.
[20] J.M. Dowling, J.W. Martin, Acta Metallurgica 24 (1976) 1147-1153.
[21] K. Strobel, M.A. Easton, L. Sweet, M.J. Couper, J.F. Nie, Materials Transactions 52 (2011) 914-919.
[22] B. Milkereit, N. Wanderka, C. Schick, O. Kessler, Materials Science and Engineering A 550 (2012) 87-96.
[23] B. Milkereit, M.J. Starink, Materials & Design 76 (2015) 117-129.
[24] J.L. Cavazos, R. Colas, Materials Science and Engineering A 363 (2003) 171-178.
[25] C. Panseri, T. Federighi, Acta Metallurgica 8(4) (1960) 217-238.
[26] F.D. Fischer, J. Svoboda, F. Appel, E. Kozeschnik, Acta Materialia 59 (2011) 3463-3472.
[27] A. Falahati, P. Lang, E. Kozeschnik, Materials Science Forum 706-709 (2012) 317-322.
[28] P.B. Hirsch, J. Silcox, R.E. Smallman, K.H. Westmacott, Philosophical Magazine 8 (1958) 897-908.
[29] G. Thomas, Philosophical Magazine 4 (1959) 1213-1228.
[30] K.H. Westmacott, R.L. Peck, Philosophical Magazine 23 (1971) 611-622.
[31] M. Kiritani, T. Nishikawa, S. Yoshida, Journal of the Physical Society of Japan 27 (1969) 67-73.
[32] W. Sun, Y. Zhu, R.K.W. Marceau, L. Wang, Q. Zhang, X. Gao, C. Hutchinson, Science 363 (2019) 972-975.

[33] K.H. Westmacott, R.S. Barnes, D. Hull, R.E. Smallman, Philosophical Magazine 6 (1961) 929-935.
[34] R.M.J. Cotterill, R.L. Segall, Philosophical Magazine 8 (1963) 1105-1125.
[35] M. Kiritani, Journal of the Physical Society of Japan 19 (1964) 618-631.
[36] M. Liu, Q. Guo, X. Zhang, M. Wüstenhagen, J. Čižek, J. Banhart, Scripta Materialia 177 (2020) 203-207.
[37] H.S. Zurob, H. Seyedrezai, Scripta Materialia 61(2) (2009) 141-144.
[38] C. Wolverton, Acta Materialia 55 (2007) 5867-5872.
[39] R. Kobayashi, D. Giofre, T. Junge, M. Ceriotti, W.A. Curtin, Physical Review Materials 1 (2017) 053604.
[40] S. Hirosawa, F. Nakamura, T. Sato, Materials Science Forum 561-565 (2007) 283-286.
[41] J. Peng, S. Bahl, A. Shyam, J.A. Haynes, D. Shin, Acta Materialia 196 (2020) 747-758.
[42] Z.Q. Liang, C.S.T. Chang, C. Abromeit, J. Banhart, J. Hirsch, International Journal of Materials Research 103(8) (2012) 980-986.
[43] Y. Aruga, M. Kozuka, Y. Takaki, T. Sato, Metallurgical and Materials Transactions A 45A(13) (2014) 5906-5913.

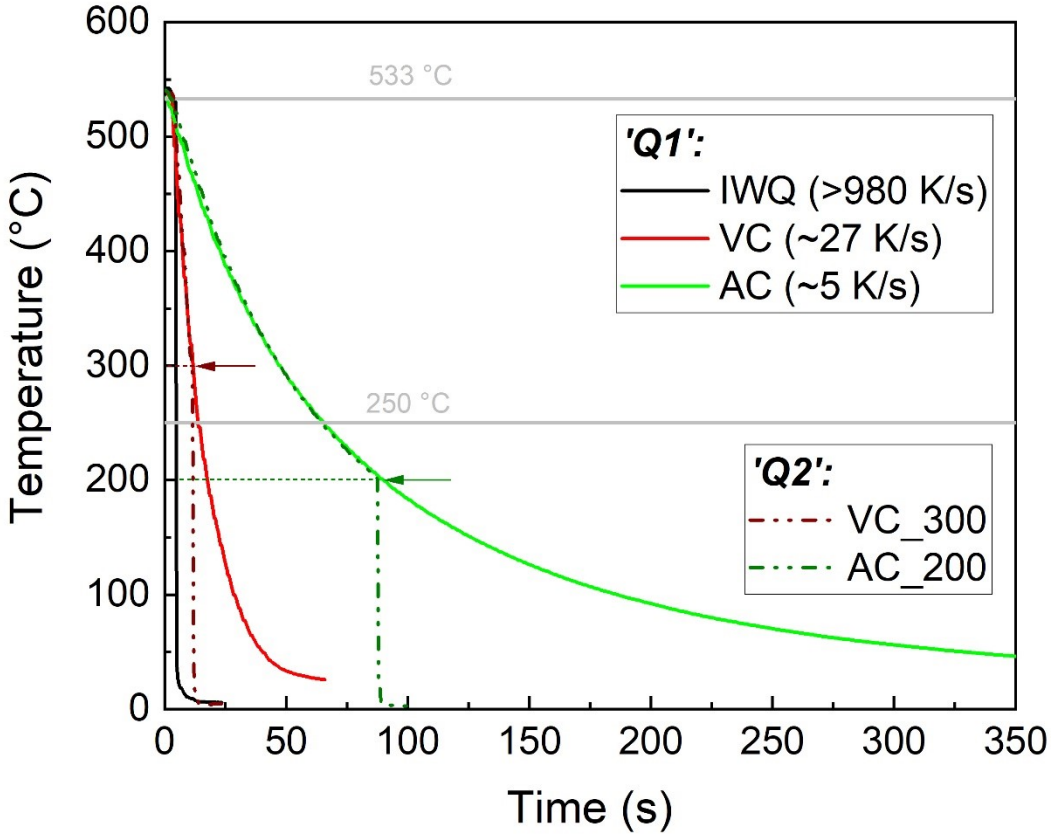

Fig. 1. Measured temperature evolution of samples during Q1-type cooling and two examples during Q2-type. Cooling rates of the Q1-type of quenching (in parentheses) are average rates between 533 °C and 250 °C.

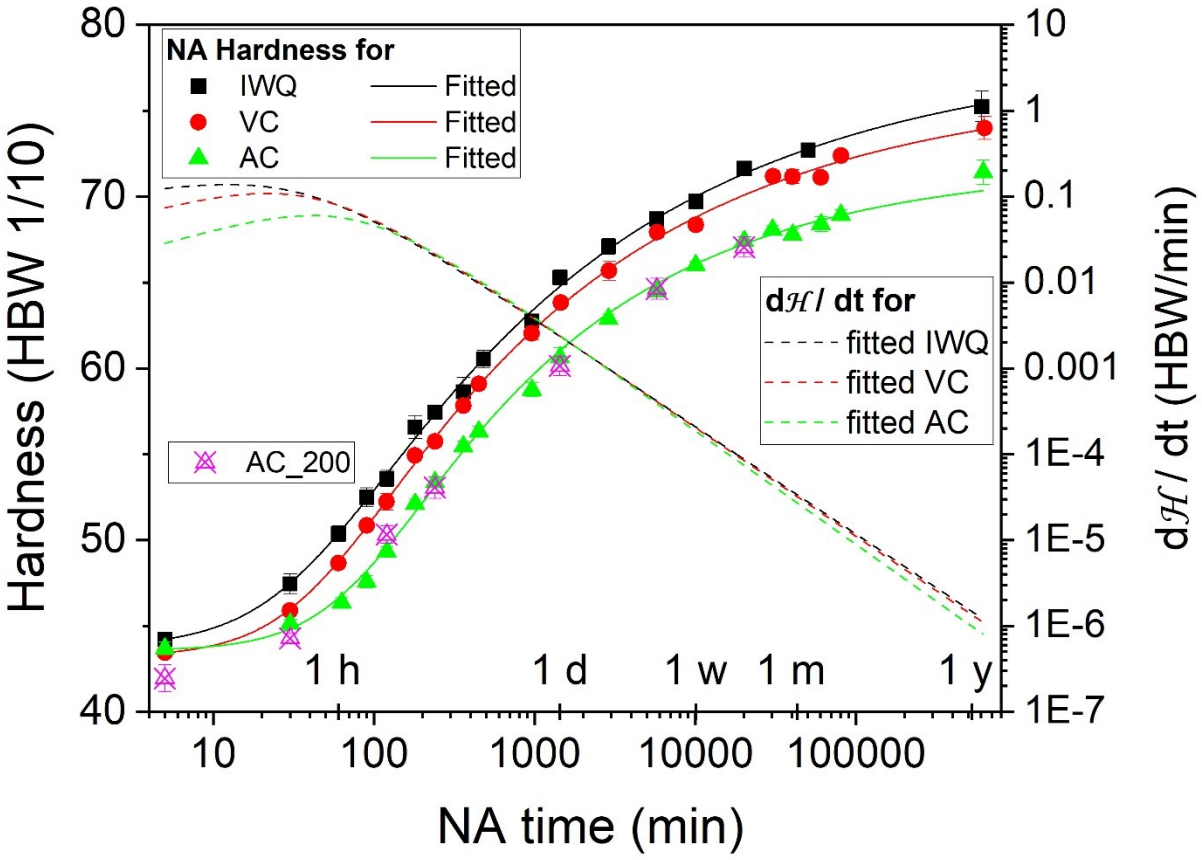

Fig. 2. Hardness of alloy during NA after various Q1-type quenches and one Q2-type quench (AC_200). Solid curves represent the data fitted by the Starink-Zahra equation: $\mathcal{H} = \mathcal{H}_0 + \mathcal{H}_1 \left\{1 - \left[\frac{(kt)^n}{\eta} + 1\right]^{-\eta}\right\}$, with $\mathcal{H}_0$ the hardness of the as-quenched state, $\mathcal{H}_1$ the maximum hardness increase during NA, t the NA time, and k, n, η the kinetic parameters [13], respectively. Initial hardness points represent NA for 5 min, which is the typical time needed for the measurement. Derivatives (hardening rate) of the fitted hardnesses are shown as dashed curves.

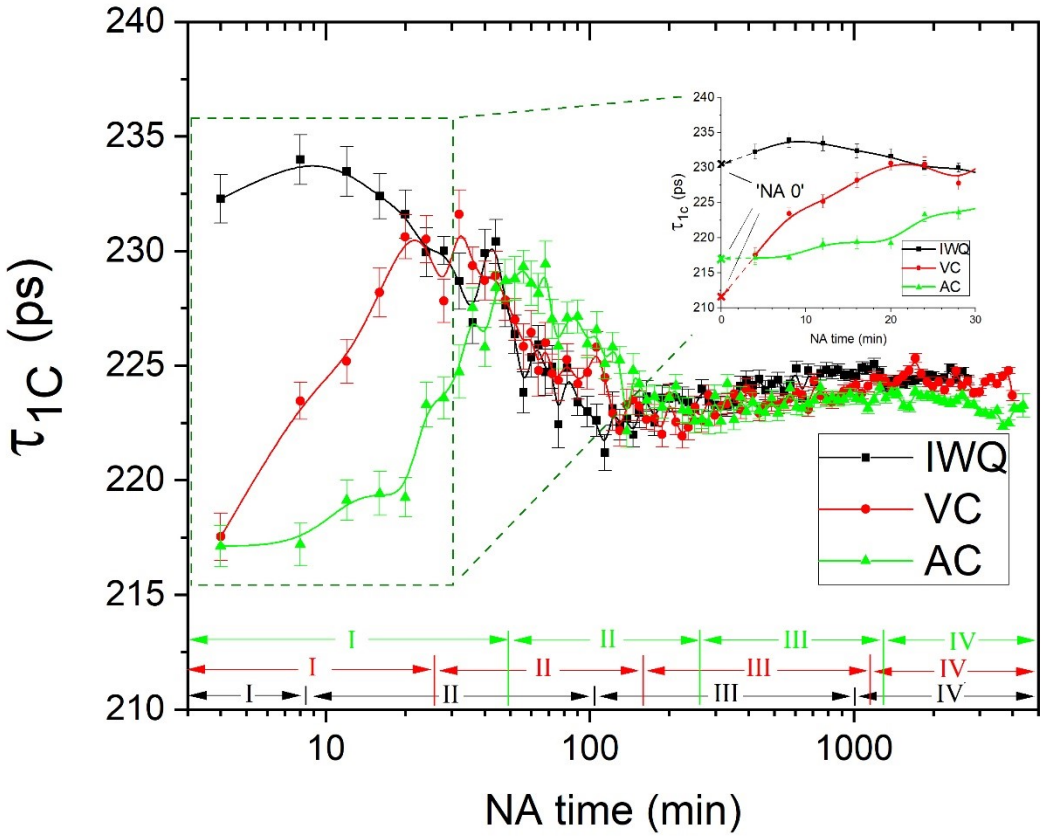

Fig. 3. One-component positron lifetimes during NA after various Q1-type quenches. The earliest lifetimes are after NA for 4 min, which is the time for sample preparation and data acquisition. Inset shows the extrapolations of the curves to zero NA time. Roman numbers (I – IV) denote various stages of positron lifetime evolution.

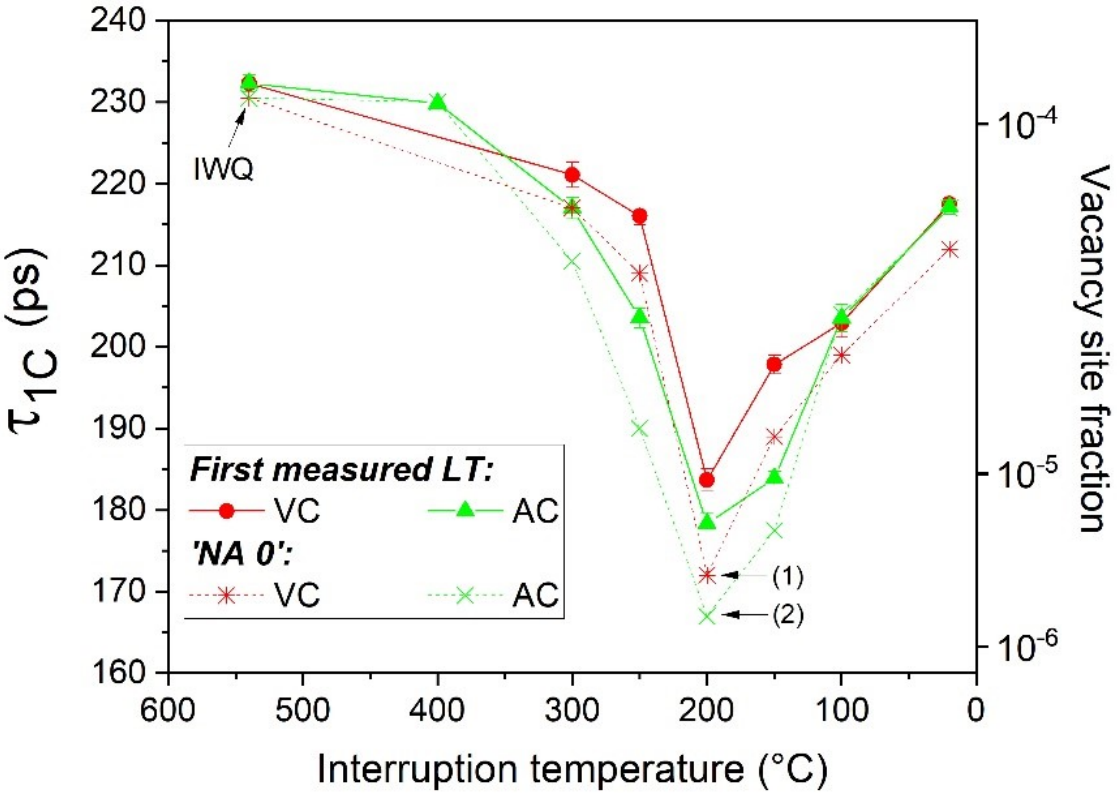

Fig. 4. One-component positron lifetime evolution during the VC and AC quenching processes. Lifetimes are measured ex-situ at room temperature after Q2-type quenching with interruption temperatures shown in the abscissa. Solid curves represent the first experimental values measured after quenching (supplementary Fig. S3), which typically took 4 – 8 min to measure at 'room temperature' due to sample preparation and data acquisition. The dashed curve gives values extrapolated to zero NA time. States (1) and (2) are further analysed in supplementary Fig. S5.

Supplementary material

SA. Details of quenching by ventilator

Fig. S1a shows the setup for ventilator cooling (VC). The samples are placed in a meshed cage during solution heat treatment. To perform cooling the sample cage is taken out of the furnace held at 540 °C and mounted on the stand against blowing air within ~1 s. The height of the stand and the distance to the ventilator are fixed so that every time cooling is conducted the same position relative to the ventilator is taken. Nine samples are quenched in every batch and there are three non-equivalent positions in the cage as illustrated in Fig. S1b. The average cooling rates (from 533 °C to 250 °C) measured at the three positions are 27.2±1.3, 27.4±1.7, and 27.8±0.8 (in $K \cdot s^{-1}$) for 1, 2 and 3 respectively, where the error margins are based on three different experiments. Thus, quenching in this device is well reproducible and the same for all 9 samples.

(a)

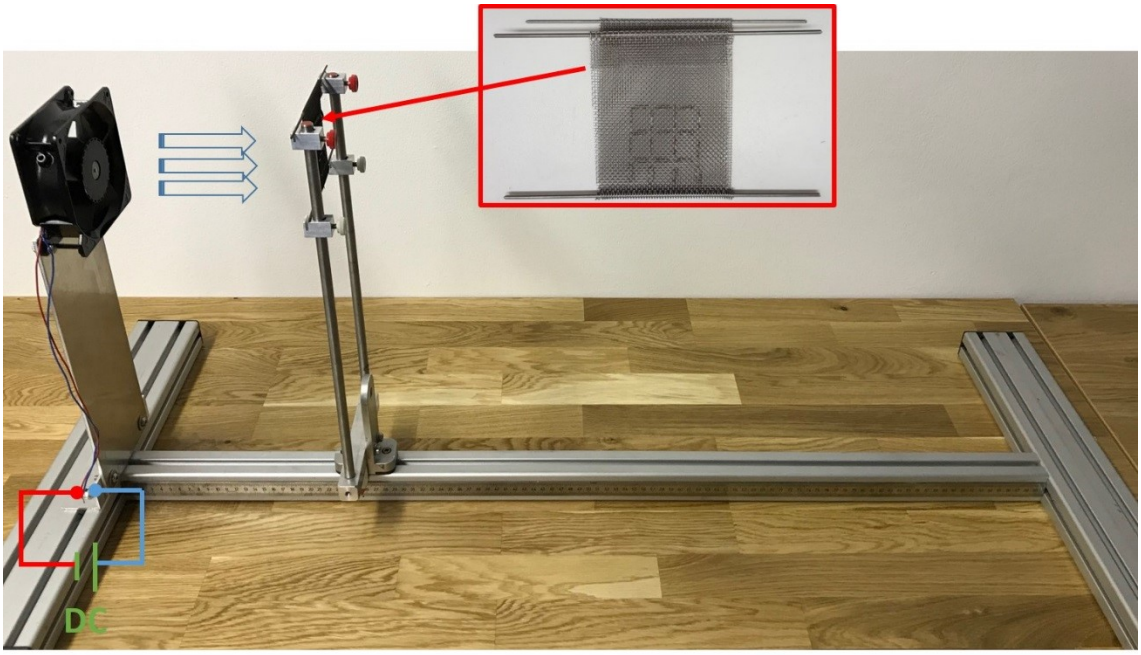

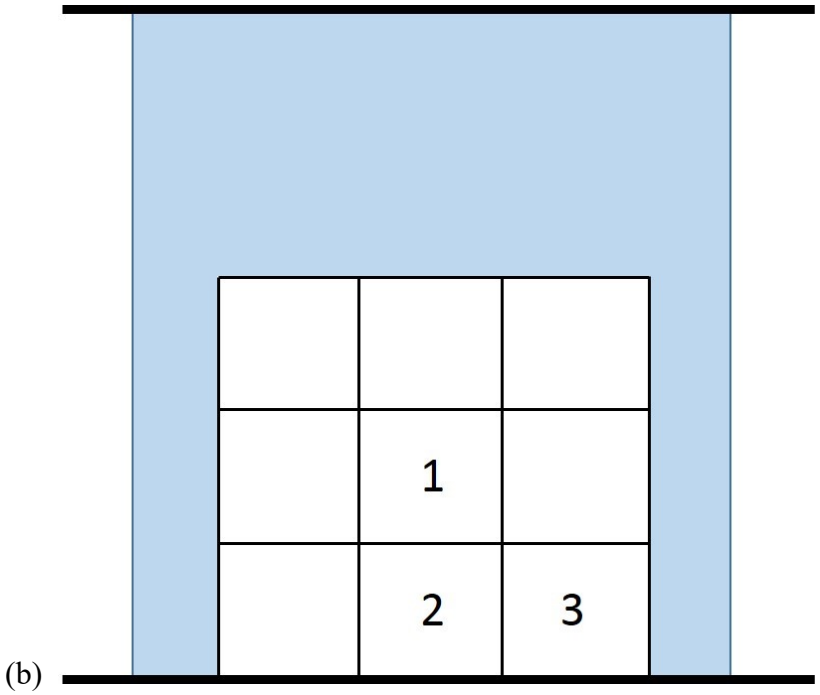

Fig. S1. (a) Cooling setup for ventilator cooling (VC) including the sample cage (in red box). (b) Schematic of the sample cage and the various non-equivalent sample positions: ‘1’ for centre (axis of ventilator), ‘2’ for edge, and ‘3’ for corner.

SB. Positron lifetimes of Al-Mg alloy after Q1-type quenches

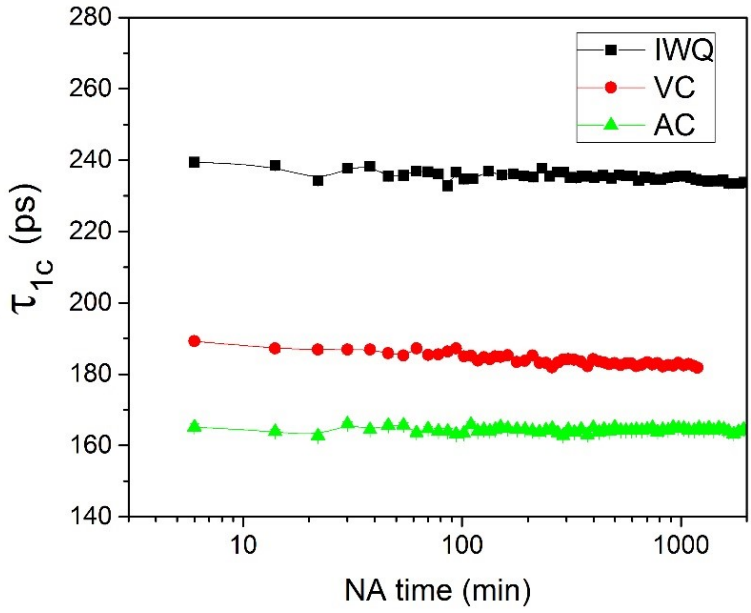

Fig. S2. Positron lifetimes τ_{1C} during NA of binary Al-0.5Mg (wt.%) alloy after various Q1-type quenches.

Fig. S2 displays the positron lifetime evolution in a binary Al-Mg alloy after quenching. It is the analogue to the measurements in Fig. 3. During NA, very little evolution of τ_{1C} is observed. The quenching rate, however, has a pronounced influence on the value of τ_{1C}. After fast quenching, vacancies are efficiently trapped by the Mg atoms, which explains values around 240 ps. During the slowest quenching, in contrast, vacancies can escape from the alloy and a very low value close to 165 ps is observed. This value is similar to that of state AC_200 in Fig. 7b, which was described as a state containing only few vacancies and clusters. Thus, during slow cooling most vacancies are not retained by the Mg atoms and can reach sinks as vacancy-Mg binding is weak well above 'room temperature'.

SC. PALS measurements of Q2-type quenched samples during NA

Fig. S3 shows how positron lifetimes evolve at 'room temperature' after slow quenches (VC and AC) from 540 °C that were interrupted at a given temperatures (100 °C to 400 °C) by a fast IWQ quench to preserve the configuration. Most curves feature an initially low value of τ_{1c}, a subsequent increase and a merger into a curve that is almost the same for all the experiments including those in Fig. 3. The insets show the data used for the extrapolation to zero NA time on a linear time scale.

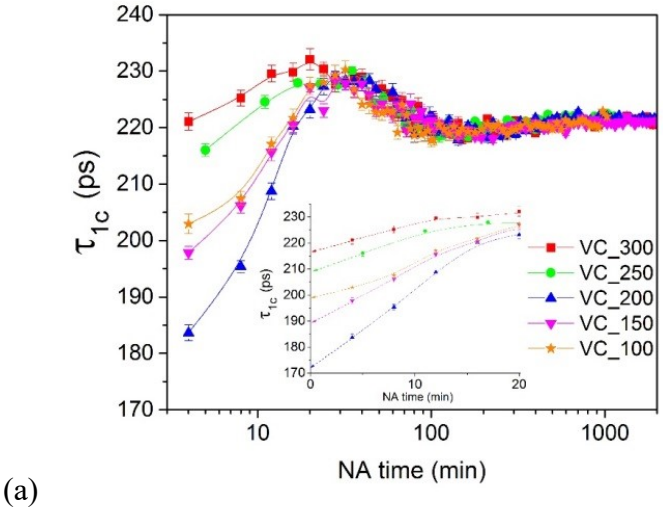

(a)

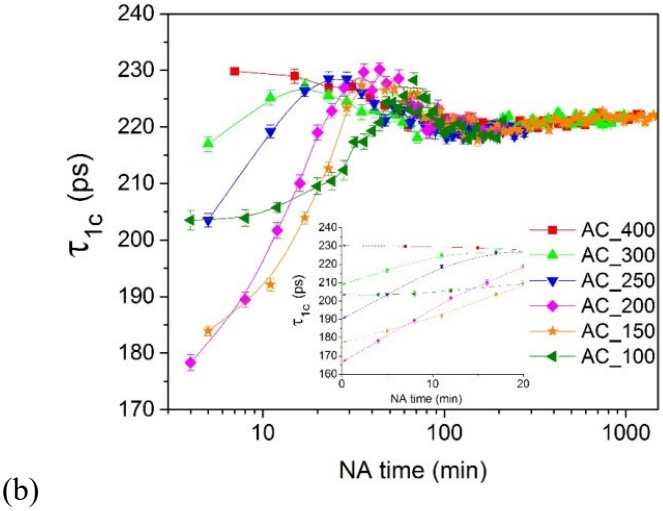

(b)

Fig. S3. Positron lifetimes τ_{1c} during NA of samples quenched in a Q2 fashion as shown in Fig. 1 for (a) VC, and (b) AC.

SD. TEM microstructure after various quenching (Q1) and influence on AA hardening

TEM was performed on samples after all three Q1-type quenches (Fig. S4a – c) on a Philips CM30 unit. Observation was conducted in the ⟨100⟩ directions of the Al matrix. Special attention was paid to secondary particles in the microstructure. Only one type of particle, named P1, can be observed in the microstructure of the IWQ sample, while at least two types of particles, P1 and P2, can be seen for VC and AC. EDX analysis reveals that P1 contains primarily Fe, Si and Mn beside Al, while P2 consists of mainly Mg and Si. P1 particles are observed in many shapes, mostly spherical or ellipsoidal, whereas P2 particles are mostly rod-shaped and are aligned along ⟨100⟩ directions of the Al matrix. Moreover, P2 particles are mostly attached to P1 or are observed at grain boundaries.

Precipitate formation during VC and AC leads to a reduction of solute supersaturation and consequently to a lower hardening after AA for 30 min or 240 min (peak-age), see Fig. S4d. This is in accordance with previous literature [1]. The formation of clusters during quenching below 200 °C increases hardness in the as-quenched state only marginally (from VC_200 to VC and AC_200 to AC) and has no pronounced influence on AA hardening.

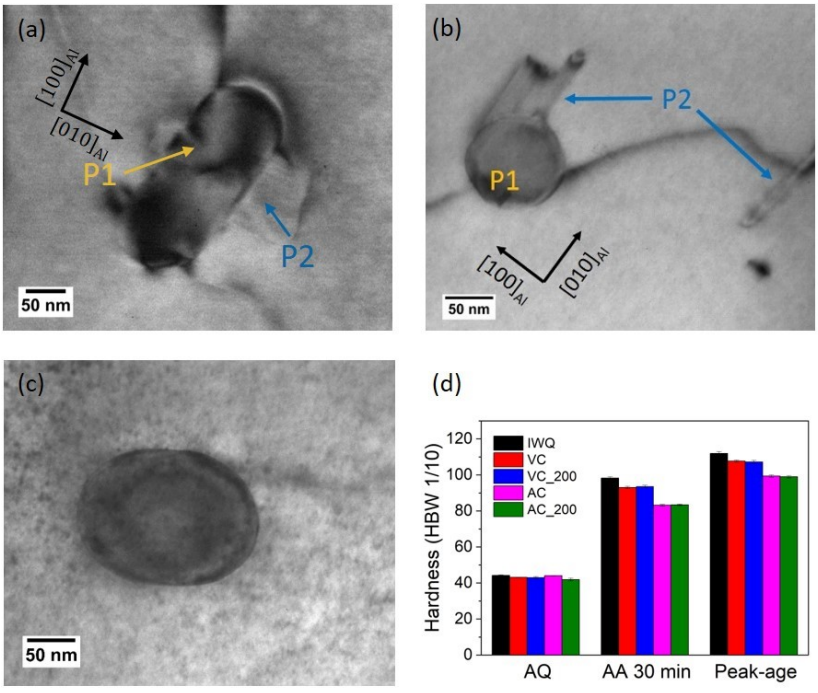

Fig. S4. (a – c) Bright-field TEM images of samples after (a) AC, (b) VC, (c) IWQ. (d) Hardness after various quench routes and subsequent AA conditions. AQ: as-quenched; Peak-age: AA for 240 min.

SE. Vacancy site fraction calculation from positron lifetime

Calculating vacancy fractions from positron lifetime data usually requires decompositions of lifetime spectra into 2 or more components. In this work, we measure τ_{1c} only which, however, is very close to the average positron lifetime that one would calculate from individual components:

$$\tau_{1c} \approx \bar{\tau} = I_0\tau_0 + I_v\tau_v, \quad I_0 + I_v = 1, \tag{1}$$

where the index 0 refers to the reduced bulk lifetime and v to annihilation in vacancy-related defects. $\tau_v = 245$ ps is assumed. By applying the equations of the two-state trapping model [2]:

$$\tau_0 = \frac{1}{\frac{1}{\tau_B} + \kappa_v}, \tag{2}$$

$$I_v = \frac{\kappa_v}{\frac{1}{\tau_B} - \frac{1}{\tau_v} + \kappa_v}, \tag{3}$$

where τ_B =160 ps is the lifetime in defect-free aluminium, and κ_v is the positron trapping rate of the vacancy-related defect. A relationship applies between κ_v and the site fraction of the vacancies x_v:

$$x_v = \frac{\kappa_v}{\mu}, \tag{4}$$

where μ is the positron trapping coefficient of a vacancy in aluminium. By combining (1 – 4) we eventually obtain the vacancy site fraction

$$x_v = \frac{\tau_B - \bar{\tau}}{\mu\tau_B(\bar{\tau} - \tau_v)}. \tag{5}$$

Using a commonly accepted value $\mu = 250\ \mathrm{ps}^{-1}$ [3] we can calculate the vacancy site fraction from the one-component positron lifetime. Fig. S5 shows the results, which, however, should not been taken too literally due to the approximations used (e.g. absence of clusters and usage of $\tau_{1c} \approx \bar{\tau}$).

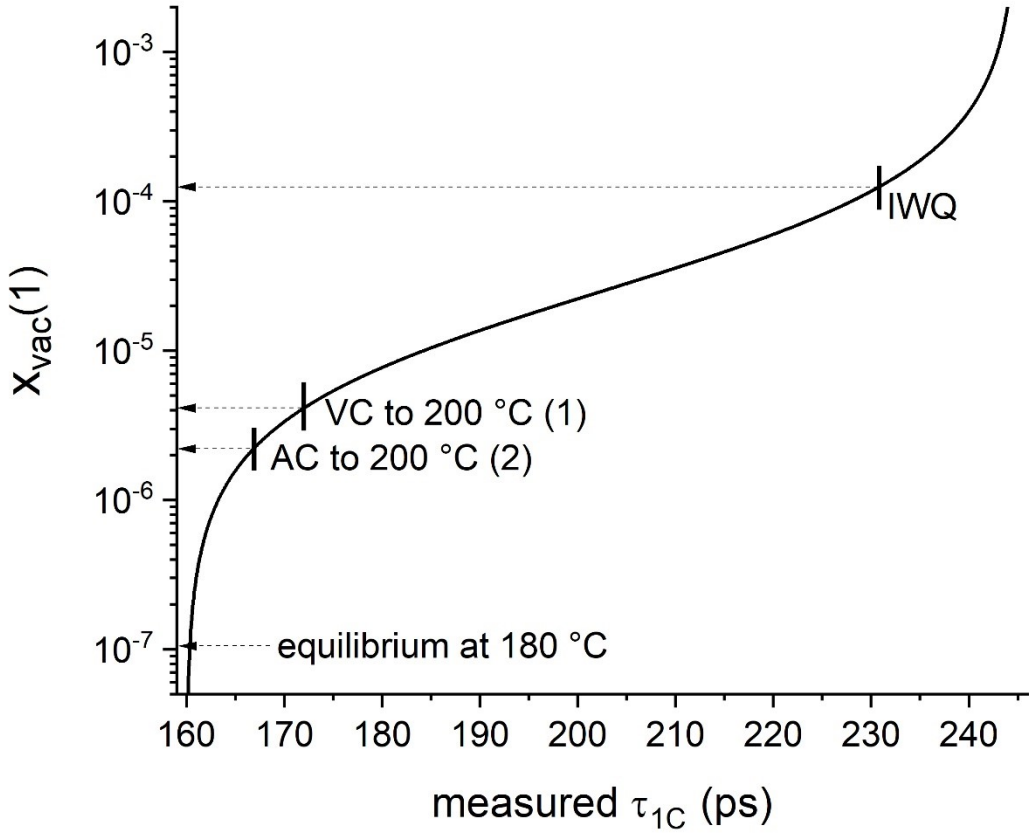

Fig. S5. Vacancy site fraction calculated using Eqs. (1-4) as a function of positron lifetime assuming validity of the positron trapping model for one trap related to vacancies characterised by a lifetime of 245 ps. The upper three arrows correspond to τ_{1C} (extrapolated to zero NA) as measured after three quenches, the lower one marks the equilibrium vacancy fraction at 180 °C as calculated from the formation enthalpy and vibrational entropy of mono-vacancies in Al [4].

References

[1] B. Milkereit, N. Wanderka, C. Schick, O. Kessler, Materials Science and Engineering A 550 (2012) 87-96.
[2] R. Krause-Rehberg, Positron Annihilation in Semiconductors, Springer, Heidelberg, 1999.
[3] J.A. Jackman, G.M. Hood, R.J. Schultz, Journal of Physics F: Metal Physics 17 (1987) 1817.
[4] T. Hehenkamp, Journal of Physics and Chemistry of Solids 55(10) (1994) 907-915.